Materials International
Open Access Journal (ISSN: 2668-5728)

*Article*
**Volume 7, Issue 2, 2025, 15**
https://doi.org/10.33263/Materials72.015

# Investigation of Silane-functionalised Magnetite Nanoparticles for Corrosion Inhibition on Mild Steel in Acidic Environments

**Geetha Pinto [1,*], Jeena Thomas [1]**

[1] Post Graduate Department of Chemistry, St Agnes College (Autonomous), Mangaluru – 575002
[*] Correspondence: geetha@stagnescollege.edu.in;

**Received: 9.11.2023; Accepted: 1.01.2025; Published: 10.06.2025**

**Abstract:** This work presents the novel synthesis of silane-functionalized $Fe_3O_4$ nanoparticles via coprecipitation, enhancing their stability for anti-corrosion applications. It uniquely investigates their effectiveness as inhibitors of mild steel in 0.5 M HCl, revealing concentration-dependent protection and highlighting the significant impact of temperature on efficiency. These insights are crucial for optimizing the use of functionalized nanoparticles in corrosion mitigation. A comprehensive investigation of their morphology and physical characteristics was conducted using field-emission scanning electron microscopy (FE-SEM) and Fourier Transform Infrared Spectroscopy (FTIR). Furthermore, the study explores the potential application of these silane-functionalized $Fe_3O_4$ nanoparticles as an anti-corrosion solution for mild steel exposed to a corrosive environment, represented by 0.5 M HCl. The findings indicate a direct correlation between inhibitor concentration and the effectiveness of corrosion inhibition. Interestingly, the protective effect of these nanoparticles diminishes as temperature rises, indicating the influence of temperature on their anti-corrosion activity. This research sheds light on the promising use of these functionalized nanoparticles to mitigate corrosion, underscoring the need for temperature-sensitive considerations in practical applications.

**Keywords:** $Fe_3O_4$ nanoparticles; aminopropyltriethoxysilane; anticorrosive activity.



## 1. Introduction

Applications for magnetic nanoparticles (MNPs) in a variety of fields, such as magnetic fluids [1], combustion [2], bioscience [3], imaging (MRI) [4], data storage, and environmental cleanup [5], are very appealing [6]. Although several effective techniques have been developed for the manufacture of magnetic nanoparticles, the stability of the particles under various conditions is crucial for successful application [7]. However, only magnetite ($Fe_3O_4$) and maghemite (-$Fe_2O_3$) NPs are primarily considered among the several types of magnetic nanoparticles (MNPs) due to their reduced toxicity for medicinal or environmental applications compared to other magnetic materials (Co- and Ni-based nanoparticles) (NPs). With a magnetic moment of 2.5 B/f.u. (formula units) for ϒ-$Fe_2O_3$ and 4.0 B/f.u. for $Fe_3O_4$, respectively, both iron oxides are ferrimagnetic [8,9].

In single-domain magnetic nanoparticles, superparamagnetism is observed below a characteristic dimension (critical diameter ds) when the thermal energy exceeds the anisotropy energy, allowing the magnetization vector to fluctuate easily between up and down states with a time-averaged net moment of zero. The temperature at which a transition from the spin-flip-

free state to the blocked state is observed is called the blocking temperature, and the time required to change from the up to the down state is called the relaxation time. The blocking temperature for a given system of NPs may vary depending on the technique, as the equipment used to perform a measurement affects the time required to complete it. The superparamagnetic state, which is typically used for the aforementioned applications, is characterized by a coercivity of zero. Because of their greater magnetic moment and relatively straightforward synthetic processes, $Fe_3O_4$ NPs are currently favored over ϒ-$Fe_2O_3$ ones. These NPs are frequently employed as the foundation for complicated functionalization to achieve various characteristics. Before the ultimate functionalization, a magnetic core and one or more intermediary coatings comprise a typical "nano-architecture"[10,11].

Due to the large surface area of magnetite nanoparticles, several active sites could be created. However, through the agglomeration, the creation of $Fe_3O_4$ nanoparticles was crucial in reducing the active sites. When the core of functionalized "nano-architectures" needs to be protected from oxidation/corrosion processes or when hazardous or pollution problems come from the core, polymer or inorganic coatings are typically used [12]. Moreover, the application of inorganic coatings (silica, alumina, or titania) enhances the stability of magnetic NPs in solution, limiting or preventing the formation of agglomerates due to magnetic dipole interactions. However, this process is constantly time-consuming and fairly expensive [13]. For instance, toxic heavy metals or molecules originating from relatively large amounts of wastewater could be captured using functionalized magnetic nanoparticles; in this case, it would be highly advised to produce functionalized NPs quickly and cheaply.

So, the objective of the current study is to functionalize magnetite nanoparticles (NPs) with an organo-silane molecule (OSM), namely 3-aminopropyltriethoxysilane (APTES). The method involves using an intermediate silica coating with the silane derivative ($Fe_3O_4$@$SiO_2$) and (3-aminopropyl)triethoxysilane (APTES) as a reagent to produce the desired functionalization. The path is shown in the following equations (1 ) & (2):

$$Fe_3O_4 + OSM \rightarrow Fe_3O_4@OSM \quad (1)$$
$$Fe_3O_4 + APTES \rightarrow Fe_3O_4@SiO_2 \quad (2)$$

In order to verify the achieved functionalization and its efficiency, the different characterizations have been analyzed by field emission scanning electron microscopy (FE-SEM) and FTIR spectroscopy [8,15,16].

## 2. Materials and Methods

Ferric chloride hexahydrate (Merk, 98%), ferrous chloride tetrahydrate (Merk, 98%), sodium hydroxide (Merk, 99.5%), aminopropyl triethoxysilane (APTES) (Merk, 98%), and distilled water were used as the primary chemicals in this study.

### *2.1. Method for synthesis of $Fe_3O_4$ nanoparticles.*

$Fe_3O_4$ nanoparticles were created using the chemical coprecipitation technique. $FeCl_3$•$6H_2O$, $FeCl_2$•$4H_2O$, and deionized water were combined to create a 0.1M ferric salt solution and a ferrous salt solution in a cleaned standard flask. These two solutions were then combined at room temperature in a 1:2 ratio. Distilled deionized water was then filled with the combination. Sodium hydroxide solution was added dropwise to the mixture while it was vigorously agitated at 500 rpm for about 30 minutes, or until a black precipitate began to form.

To ensure the formation and growth of magnetic nanoparticles, the solution was subjected to magnetic stirring for 60 minutes. To ensure that any remaining salts were removed, the precipitate was rinsed with deionized water and filtered through the Whatman No. 41 filter paper. The precipitate was then dried after further rinsing with ethanol to remove any residual salts.

*2.2. Method for preparation of silane functionalized $Fe_3O_4$ nanoparticles.*

Silane-functionalized $Fe_3O_4$ nanoparticles were synthesized by using the same procedure used for the synthesis of $Fe_3O_4$ nanoparticles. Then, it was added with 10 ml of aminopropyl triethoxysilane. The mixture was stirred vigorously for about 30 minutes under a magnetic stirrer. The precipitate was filtered and washed with ethanol. Finally, silane-functionalized $Fe_3O_4$ nanoparticles were dried in the oven.

*2.3. Methods for corrosion rate measurement.*

2.3.1. Electrochemical impedance spectroscopy (EIS) measurements.

The electrochemical measurements were performed using an electrochemical workstation, Gill Ac Serial No. 1864 (ACM instruments). The measurements were carried out using a conventional three-electrode Pyrex glass cell with a saturated calomel electrode (SCE) as the reference electrode, a platinum electrode as an auxiliary electrode, and a mild steel coupon as the working electrode. The potentials were measured with respect to the reference electrode. The working electrode was immersed in the test solution for 30 min to establish a steady state open circuit potential ($E_{ocp}$). Electrochemical measurements were performed after measuring the Eocp. The impedance studies were conducted at the OCP by varying the frequency between 100 kHz and 0.01 Hz. Impedance spectra were recorded at 10mV amplitude, and data were analyzed using Nyquist plots. The charge transfer resistance, $R_{ct}$, was obtained from the diameter of the semicircle in the Nyquist plot. From the value of $R_{ct,}$ the value of percentage inhibition efficiency (η) of the inhibitor was calculated using equation (3).

$$\eta(\%) = \frac{R_{ct} - R_{ct}^{\circ}}{R_{ct}} \times 100 \qquad (3)$$

Where $R_{ct}$ and $R_{ct}$ are the charge transfer resistances in the presence and in the absence of inhibitors [17].

2.3.2. Potentiodynamic polarization (PDP) measurements.

Potentiodynamic polarization measurements were carried out by using Gill AC software in a Pyrex cell equipped with a conventional three-electrode assembly. The polished specimen was exposed to the corrosion medium of different concentrations at different temperatures (30°C – 50°C) and allowed to attain a steady open circuit potential. The potentiodynamic curves were recorded by polarizing the specimen to -250 mV cathodically and +250 mV anodically with respect to the open circuit potential (OCP) at a scan rate of 1 mV $s^{-1}$. Electrochemical polarization parameters were evaluated using the Tafel plots. The percentage inhibition efficiency (η) was calculated using equation(4)

$$\eta(\%) = \frac{\mathbf{i_{corr} - i_{corr(inh)}}}{\mathbf{i_{corr}}} \times 100 \qquad (4)$$

Where $i_{corr(inh)}$ and $i_{corr}$ are the corrosion current densities with and without the inhibitors.

## 3. Results and Discussion

The characterization techniques used for this study are a Fourier transform infrared (FT-IR) spectrometer, done using Thermo Fischer Nicolet IS5 (USA), Scanning electron microscopy (SEM) done using FEI Nova Nano FESEM 450, and a corrosion inhibition study was performed using an electrochemical work station Gill Ac Serial No. 1864 (ACM instruments).

### *3.1. Characterization.*

#### 3.1.1. Scanning electronic microscopy (SEM).

Using SEM, the surface morphology of mild steel was studied. Figures 1a and 1b depict the SEM images of the sample in the absence and presence of 1000 ppm of $Fe_3O_4$@APTES nanoparticles after 3 hours of immersion in 0.5M HCl. Few surface pits are visible in the absence of an inhibitor due to rapid corrosion in an acidic solution. The surface is free of pits and cracks when $Fe_3O_4$@APTES nanoparticles are present. The SEM image demonstrates the spherical shape of the APTES functionalized $Fe_3O_4$ nanoparticles. Inhibitor molecules coat the specimen, forming a protective layer that shields the surface from corrosion.

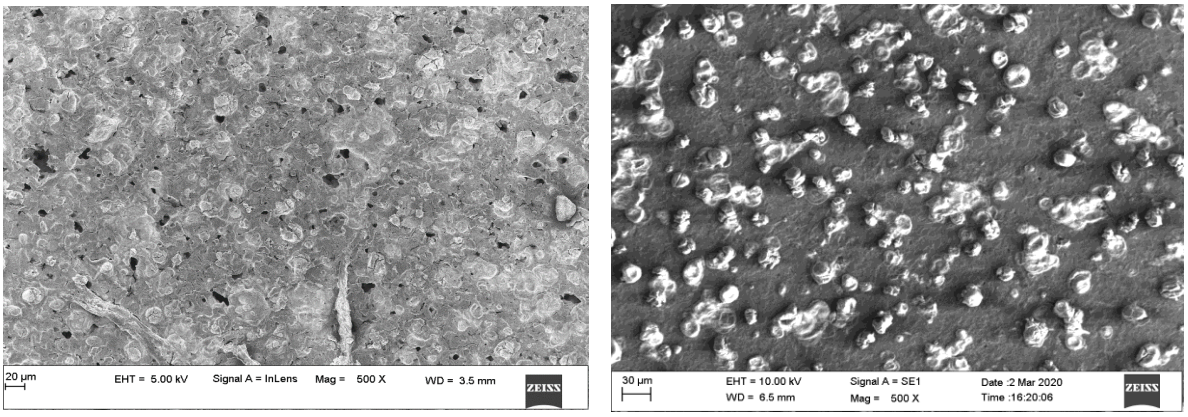


**(a)** **(b)**

**Figure 1. (a)** SEM micrographs of mild steel surface exposed to 0.5M HCl; **(b)** SEM micrographs of mild steel surface exposed to 0.5M HCl and 1000 ppm silane functionalized $Fe_3O_4$ NPs.

#### 3.1.2. Fourier transform infrared spectroscopic study.

Figure 2 displays the FT-IR spectra of APTES-functionalized $Fe_3O_4$ nanoparticles. The peak at 3258.45 $cm^{-1}$ is related to the stretching vibrations of OH adsorbed on the surface of the $Fe_3O_4$ nanoparticles, while the strong adsorption at 631.36 $cm^{-1}$ is attributed to the stretching of Fe-O. By appearing at 2849.49 $cm^{-1}$ and 2917.65 $cm^{-1}$, C-H stretching vibrations proved the presence of the propyl group of APTES. The Si-O-Si group is present in the band at 1096 $cm^{-1}$. Furthermore, N-H stretching can be seen in the peaks at 3258.45 $cm^{-1}$ and 3352.91 $cm^{-1}$.

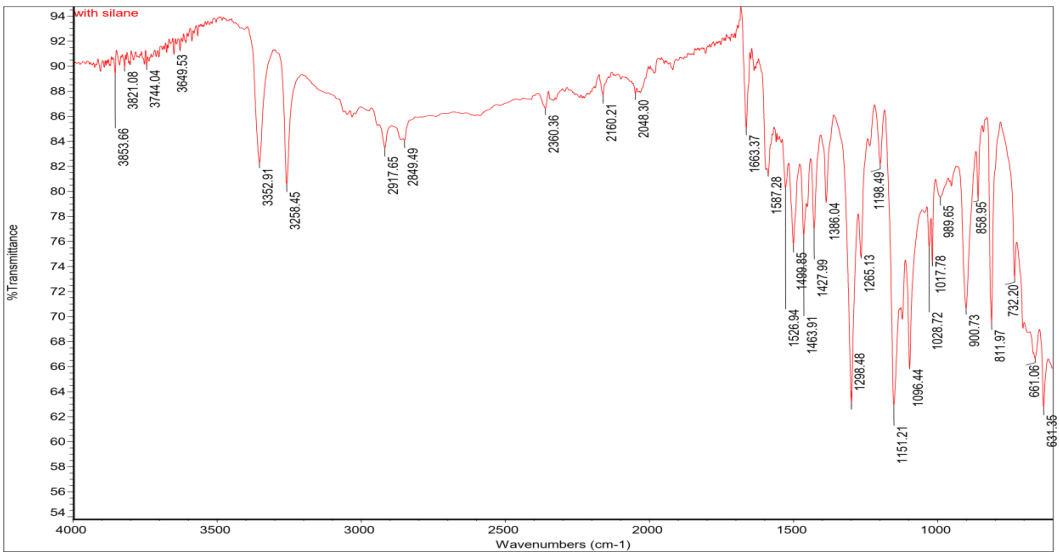


**Figure 2.** FT-IR spectrum of APTES functionalized $Fe_3O_4$ nanoparticles.

*3.2. Corrosion inhibition studies.*

3.2.1. Potentiodynamic polarization (PDP) measurements.

Figure 3 displays the potentiodynamic polarisation curves for mild steel corrosion in 0.5 M HCl with and without various concentrations of silane-functionalized magnetite nanoparticles at 30°C. Curves with a similar shape were also found at other temperatures.

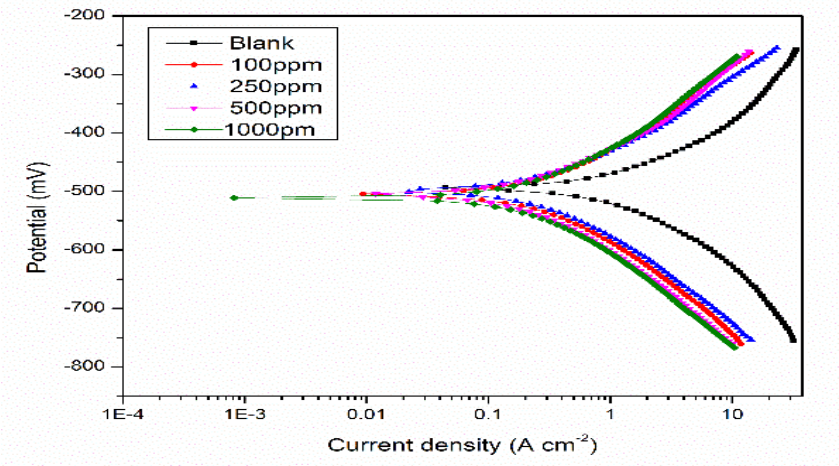


**Figure 3.** Tafel plots for the corrosion of mild steel in 0.5M HCl in the presence of different concentrations of APTES functionalized $Fe_3O_4$ nanoparticles at 30°C.

Table 1 lists the electrochemical characteristics from the plots, including corrosion potential ($E_{corr}$), corrosion potential density ($i_{corr}$), and Tafel constants ($\beta_a$ and $\beta_c$).

**Table 1.** Results of potentiodynamic polarization studies on mild steel in 0.5M HCl containing different concentrations of APTES functionalized $Fe_3O_4$ nanoparticles at different temperatures.

| Temp. (°C) | Conc. of inhibitor (ppm) | $i_{corr}$ (mA/cm$^2$) | $\beta_a$ (mVdec$^{-1}$) | $\beta_c$ (mVdec$^{-1}$) | $E_{corr}$ (mV/SCE) | CR (mm/yr) | IE (%) |
|---|---|---|---|---|---|---|---|
| 30 | Blank | 1.53 | 138.81 | 161.59 | -495.4 | 18.174 | |
| | 100 | 0.39 | 155.23 | 167.06 | -505.3 | 4.619 | 74.58 |
| | 250 | 0.33 | 122.46 | 149.58 | -498.2 | 3.936 | 78.33 |
| | 500 | 0.29 | 128.47 | 164.11 | -505.7 | 3.492 | 80.78 |
| | 1000 | 0.21 | 124.73 | 141.9 | -510.6 | 2.566 | 85.87 |

| Temp. (°C) | Conc. of inhibitor (ppm) | $i_{corr}$ (mA/cm$^2$) | $\beta_a$ (mVdec$^{-1}$) | $\beta_c$ (mVdec$^{-1}$) | $E_{corr}$ (mV/SCE) | CR (mm/yr) | IE (%) |
|---|---|---|---|---|---|---|---|
| 35 | blank | 1.62 | 125.63 | 144.52 | -494.1 | 19.20 | |
| | 100 | 0.66 | 144.3 | 187.78 | -504.3 | 7.809 | 59.32 |
| | 250 | 0.52 | 132.22 | 150.12 | -503.8 | 6.180 | 67.80 |
| | 500 | 0.38 | 113.75 | 137.34 | -502.9 | 4.538 | 76.36 |
| | 1000 | 0.29 | 107.76 | 129.09 | -498.0 | 3.450 | 82.03 |
| 40 | blank | 1.72 | 123.71 | 157.76 | -485.3 | 20.363 | |
| | 100 | 0.76 | 145.36 | 176.56 | -503.8 | 9.024 | 55.68 |
| | 250 | 0.67 | 141.49 | 157.27 | -501.8 | 7.925 | 61.07 |
| | 500 | 0.55 | 126.98 | 136.81 | -504.0 | 6.525 | 67.95 |
| | 1000 | 0.49 | 120.74 | 136.21 | -503.7 | 5.801 | 71.50 |
| 45 | blank | 1.95 | 99.85 | 142.07 | -474.3 | 23.126 | |
| | 100 | 0.90 | 142.89 | 176.55 | -500.5 | 10.685 | 53.79 |
| | 250 | 0.83 | 149.09 | 184 | -503.8 | 9.857 | 57.37 |
| | 500 | 0.64 | 125.77 | 146.26 | -500.0 | 7.648 | 66.92 |
| | 1000 | 0.60 | 124.85 | 154.42 | -498.5 | 7.127 | 69.18 |
| 50 | blank | 2.45 | 94.41 | 106.44 | -469.1 | 28.427 | |
| | 100 | 1.15 | 131.25 | 127.05 | -488.7 | 13.639 | 52.95 |
| | 250 | 1.11 | 166.45 | 157.03 | -437.6 | 12.868 | 54.73 |
| | 500 | 0.99 | 154.29 | 194.3 | -445.1 | 11.478 | 59.62 |
| | 1000 | 0.76 | 129.7 | 148.48 | -502.8 | 9.059 | 68.74 |

The percentage inhibition efficiency (IE %) was calculated from equation (5).

$$\eta(\%) = \frac{i_{corr} - i_{corr(inh)}}{i_{corr}} \times 100 \qquad (5)$$

$I_{corr}$ and $I_{corr}$(inh) are the corrosion current densities in the absence and in the presence of an inhibitor, respectively. The corrosion rate is calculated using equation (6)

$$\text{Corrosion rate}(\text{mm y}^{-1}) = \frac{3270 \times M \times i_{corr}}{\rho \times Z} \qquad (6)$$

Where 3270 is a constant that defines the unit of corrosion rate, Icorr = corrosion current density in A cm$^{-2}$, ρ = density of the corroding material, 8.23 g cm$^{-3}$, M = Atomic mass of the metal, and Z = number of electrons transferred per metal atom [18].

The Figure shows that by decreasing the corrosion current densities on both polarisation curves, the addition of the investigated inhibitor inhibits both cathodic and anodic reactions and, as a result, lowers the corrosion rate. The table shows that the shift in $E_{corr}$ values lacks a clear trend, indicating that the inhibitor acts as a mixed-type inhibitor.

With increasing inhibitor concentration, inhibition effectiveness increases. Both anodic and cathodic reactions are affected, as evidenced by the changes in the anodic and cathodic Tafel slopes observed after the addition of the inhibitor. Both the hydrogen evolution reaction at the cathode and the anodic dissolution of metal are impacted by the addition of an inhibitor. According to the parallel cathodic Tafel curves, the reduction mechanism is unaffected by the presence of the inhibitors, and the hydrogen evolution is activation-regulated [19]. The βc values change with increasing inhibitor concentration, indicating the inhibitor's effect on hydrogen evolution kinetics. The inhibitor molecules adsorbed to the steel surface may be responsible for the change in the anodic Tafel slope βa [20].

Inhibition efficiency increases with increasing inhibitor concentration. This indicates that as the inhibitor concentration increases, a barrier film forms, preventing acid attack on the metal surface.

3.2.2. Effect of temperature.

The metal surface undergoes numerous changes due to temperature fluctuations, including rapid etching and desorption of the inhibitor and the inhibitor itself, which, in some cases, may undergo breakdown and/or rearrangement [21]. The calculation of numerous thermodynamic functions for inhibition and/or adsorption processes, however, is made easier and helps specify the type of adsorption for the investigated inhibitors. Corrosion potential ($E_{corr}$), anodic Tafel slope ($\beta_a$), and cathodic Tafel slope ($\beta_c$) results in this investigation are not significantly impacted by an increase in solution temperature. This shows that a temperature increase does not alter the way corrosion occurs. Yet, for both blank and inhibited solutions, $I_{corr}$ and, consequently, the specimen's rate of corrosion rise as temperature rises. As the temperature rises, the inhibition effectiveness declines, indicating the desorption of inhibitor molecules [22]. The apparent activation energy ($E_a$) for the corrosion process in the presence and absence of an inhibitor can be calculated using Arrhenius law using equation (7) [23].

$$\ln (CR) = B - \left(\frac{Ea}{RT}\right) \quad (7)$$

When the corrosion rate is plotted against the reciprocal of absolute temperature, 1/T, a straight line is produced with a slope of $-E_a/R$, which represents the activation energy for the corrosion process. Figure 4 (a) displays the Arrhenius graphs for the mild steel specimen. Figure 4 (b) displays the relationship between ln(corrosion rate/T) and 1/T for mild steel samples at varied inhibitor concentrations in 0.5 M hydrochloric acid.

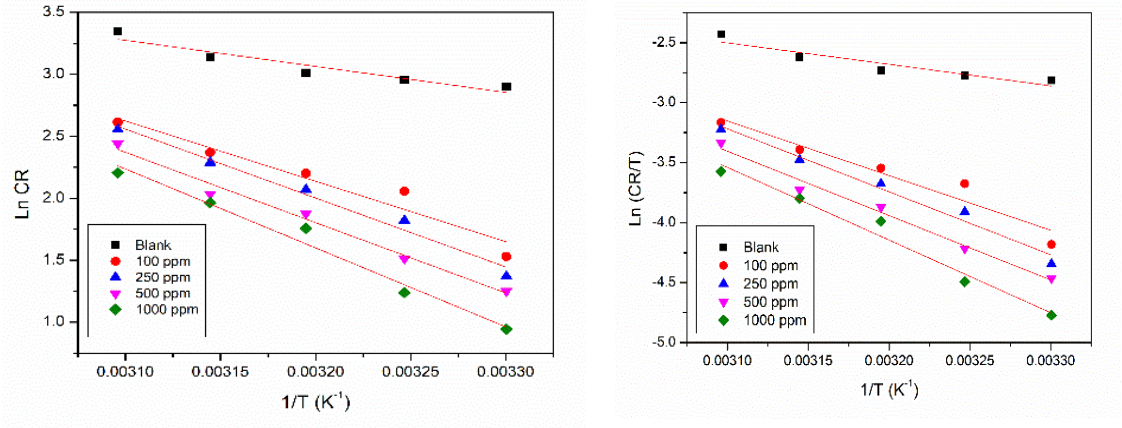


(a) (b)

**Figure 4**. (a) Arrhenius plots for the dissolution of mild steel in 0.5 M hydrochloric acid containing different concentrations of inhibitor; (b) ln(CR)/T versus 1/T for aged mild steel in 0.5 M hydrochloric acid containing different concentrations of inhibitor.

The entropy and enthalpy of activation values for the dissolution of steel were calculated from the transition state theory equation (8).

$$CR = (RT/Nh)\exp(\Delta S_a/R)\exp(-\Delta H_a/RT) \quad (8)$$

where h is Plank's constant, and N is Avagadro's number. A plot of ln(CR/T) versus 1/T gives straight line with slope = $-\Delta H_a/R$ and intercept = $\ln(R/Nh) - \Delta S_a/R$.

The calculated values of $\Delta H^{\#}$ and $\Delta S^{\#}$ are given in Table 2.

**Table 2.** Activation parameters for the corrosion of aged mild steel in 0.5 M hydrochloric acid containing different concentrations of inhibitor.

| Conc. of inhibitor (ppm) | Ea (kJ mol$^{-1}$) | $\Delta H^{\#}$ (kJ mol$^{-1}$) | $\Delta S^{\#}$ (J mol$^{-1}$ K$^{-1}$) |
|---|---|---|---|
| Blank | 17.48 | 14.88 | -172.18 |
| 100 | 40.47 | 37.87 | -106.34 |
| 250 | 46.24 | 43.64 | -88.99 |
| 500 | 47.18 | 44.58 | -87.63 |
| 1000 | 52.96 | 50.35 | -70.85 |

Chemically stable surface-active inhibitors raise the activation energy and reduce the amount of corrosion-prone surface area [24]. In a 0.5 M hydrochloric acid solution with an inhibitor, the activation energy ($E_a$) value is higher than it would be without an inhibitor. The extent of the increase is proportional to the inhibitor concentration, suggesting that as the inhibitor concentration rises, so does the energy barrier for the corrosion reaction. The rise in activation energy $E_a$ may be due to the physical adsorption of the inhibitor [25], which results in the enhancement of surface coverage with the rise in the inhibitor concentration. An appreciable decrease in the inhibitor's adsorption on the metal surface with an increase in temperature. The reason for the inhibitor's lower inhibitory effectiveness may be a comparable rise in corrosion rate brought on by more metal being exposed to the acid [26].

Entropy levels for activation are high and negative in both the absence and presence of an inhibitor. This suggests that the activated complex in the rate-determining step represents an association step rather than a dissociation step, thereby reducing randomness when switching from reactants to activated complexes [27]. The entropy of activation values for inhibited solutions is less negative than those for uninhibited solutions. This shows that as one transitioned from reactants to the activated complex, unpredictability increased. This could be caused by the adsorption of organic inhibitor molecules from the acidic solution, which could be thought of as a quasi-substitution process between the organic substance in the aqueous phase and water molecules at the electrode surface [28].

3.2.3. Adsorption studies.

Corrosion inhibitors have been shown to reduce metal dissolution by adhering to the metal/corrosive medium interface and forming a barrier that prevents the metal surface from contacting the corrosive medium. The adsorption pathway is typically thought of as a substitution process between water molecules adsorbed at the metal surface, $H_2O$ (ads) and the inhibitor in the aqueous solution Inh(sol) described below by the equation (9) 9.

$$\mathrm{Inh}_{Sol} + x\mathrm{Inh}_{Sol} \leftrightarrow \mathrm{Inh}_{ads} + xH_2O_{sol} \quad (9)$$

Where $x$ represents the number of water molecules replaced by one molecule of adsorbed inhibitor, the linear relationship between surface coverage (h) value and Cinh must be discovered in order to generate the isotherm. Many isotherms, including the Langmuir, Temkin, Frumkin, and Flory-Huggins isotherms, were tried to fit the h values. By far, the modified Langmuir adsorption isotherm produces the best fit. The following equation (10)10 can be used

$$\frac{\mathbf{C_{inh}}}{\boldsymbol{\theta}} = \mathbf{C(inh)} + \frac{\mathbf{1}}{\mathbf{K_{ads}}} \quad (10)$$

Where Cinh is the concentration of inhibitor, K is the equilibrium constant for the adsorption process, and θ is the degree of the surface coverage, which is calculated using the following equation (11).

$$\boldsymbol{\theta = \frac{IE\%}{100}} \quad (11)$$

Where IE% is the percentage inhibition efficiency, the plot of Cinh/h versus Cinh gives a straight line with intercept 1/K, as shown in Figure 5.

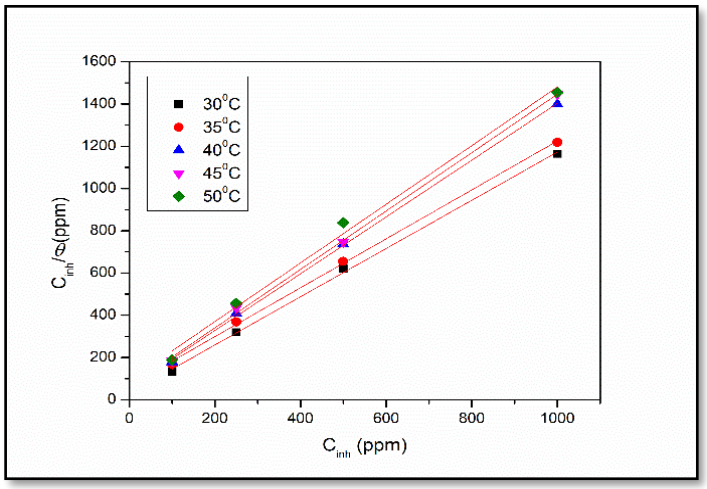


**Figure 5.** Langmuir adsorption isotherm of APTES functionalized $Fe_3O_4$ nanoparticles on mild steel in 0.5 M HCl at different temperatures.

The standard free energy of adsorption ($\Delta G^o ads$) was obtained using equation (12).

$$\boldsymbol{K_{ads} = \frac{1}{55.5} \exp\left(\frac{-\Delta G^0_{ads}}{RT}\right)} \quad (12)$$

Where the value 55.5 is the concentration of water in solution in M (mol/L), R is the universal gas constant, and T is absolute temperature [29]. The slopes of straight lines and the linear regression coefficients are approximately equal to one, indicating that the adsorbed molecules interact little with one another and that the inhibitor adheres to Langmuir's adsorption isotherm [30]. The examined inhibitor's high K values show a significant amount of inhibitor adsorption on the alloy surface. Negative values of $\boldsymbol{\Delta G^o_{ads}}$ are the characteristic property of strong spontaneous adsorption for the examined substance. Standard free energy values of -20 kJ $mol^{-1}$ or less negative are typically linked to an electrostatic interaction between charged molecules and charged metal surfaces, leading to physisorption, and those of -40 kJ $mol^{-1}$ or more negative involve charge sharing or transfer from the inhibitor molecules to the metal surface to form a coordinate covalent bond, leading to chemisorption [31,32].

**Table 3.** Thermodynamic parameters for the adsorption of APTES functionalized $Fe_3O_4$ nanoparticles on mild steel in 0.5M HCl at different temperatures.

| Temp (°C) | $K_{ads}$ ($mol^{-1}$ L) | $\Delta G^0_{ads}$ (kJ $mol^{-1}$) | $R^2$ |
|---|---|---|---|
| 30 | 14393.07 | -34.23 | 0.998 |
| 35 | 6711.27 | -32.84 | 0.998 |
| 40 | 7612.26 | -33.70 | 0.999 |
| 45 | 7008.42 | -34.02 | 0.998 |
| 50 | 4868.96 | -33.58 | 0.990 |

In 0.5 M hydrochloric acid, the$\Delta G^{o}_{ads}$ values for the investigated inhibitor on the alloy surface vary from -30 to -34 kJ/mol, as shown in the table 3, showing both physical and chemical adsorptions [33].

3.2.4. Electrochemical impedance spectroscopy (EIS) measurements.

EIS is a potent approach for comprehending corrosion and inhibition mechanisms. Temperatures of 30-50°C were used to record the impedance diagrams for mild steel in 0.5 M HCl with and without varied concentrations of the silane-functionalized magnetite nanoparticle inhibitor. Figure S6(a) shows the Nyquist plot that was produced at 30°C. The simplest electrical equivalent circuit for explaining the electrochemical behavior of a metal in an acidic solution is Randle's circuit, given in Figure 6 (b), which consists of solution resistance (Rs), charge transfer resistance (Rct), and double-layer capacitance (Cdl). The charge transfer of the corrosion process and the time constant of the electric double layer are responsible for the high-frequency (HF) capacitive loop.

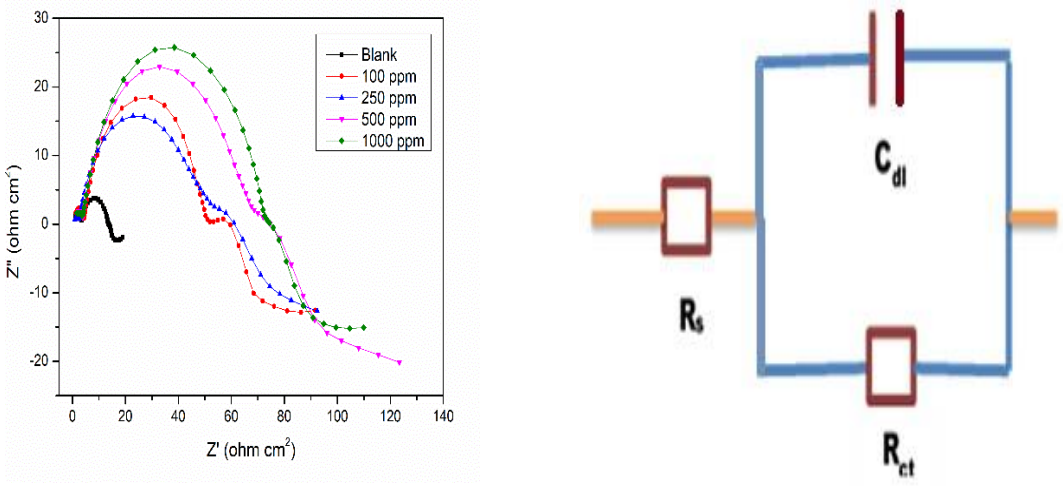


(a) (b)

**Figure 6**. (a) EIS curve for the corrosion of mild steel at different concentrations of NP's at 30°C; (b) Equivalent circuit used to fit EIS data.

The presence of an inhibitor raises the impedance but does not affect the behavior's other features. These findings confirm polarisation measurements that the inhibitor does not alter the electrochemical reactions that cause corrosion. It inhibits corrosion primarily through its adsorption on the metal surface [34]. An inductive loop is followed by a depressed capacitive loop in the low-frequency (LF) region of the impedance plots, whose width increases with an increase in inhibitor concentration. Surface roughness, the distribution of active materials, and other factors may all contribute to the depressed capacitive loop with its center below the real axis [35].

The real and imaginary components of the impedance are plotted along the X- and Y-axes, respectively, in the Nyquist plot, which displays the results of the EIS analysis [29, 30]. The inhibitor's effectiveness is calculated using the following equation (13):

$$\eta\% = \frac{\mathbf{R_{ct(inh)} - R_{ct}}}{\mathbf{R_{ct(inh)}}} \times \mathbf{100} \qquad (13)$$

where $Rct_{(inh)}$ and Rct stand for the charge transfer resistance with and without an inhibitor, respectively. The results show that the charge transfer process mostly regulates the

corrosion process as Rct values increase with the increase in inhibitor concentration, as shown in Table 4.

**Table 4.** Electrochemical impedance data for the corrosion of mild steel in 0.5M HCl containing different concentrations of APTES functionalized $Fe_3O_4$ nanoparticles carried out at different temperatures.

| Temperature of medium (°C) | Concentration of inhibitor (ppm) | $R_{ct}$ ($\Omega$ cm$^2$) | $R_s$ ($\Omega$ cm$^2$) | IE (%) |
|---|---|---|---|---|
| | blank | 10.22 | 3.29 | |
| | 100 | 44.65 | 4.18 | 77.11 |
| 30 | 250 | 46.65 | 1.88 | 78.09 |
| | 500 | 60.29 | 3.63 | 83.04 |
| | 1000 | 69.24 | 3.38 | 85.23 |
| | blank | 10.04 | 2.91 | |
| | 100 | 30.16 | 2.18 | 66.71 |
| 35 | 250 | 41.41 | 2.94 | 75.75 |
| | 500 | 44.82 | 3.23 | 77.59 |
| | 1000 | 47.06 | 2.98 | 78.66 |
| | blank | 8.259 | 2.21 | |
| | 100 | 24.88 | 2.34 | 66.80 |
| 40 | 250 | 29.71 | 3.12 | 72.20 |
| | 500 | 32.96 | 2.89 | 74.94 |
| | 1000 | 34.57 | 3.09 | 76.10 |
| | blank | 7.904 | 2.39 | |
| | 100 | 19.11 | 2.53 | 58.63 |
| 45 | 250 | 28.22 | 1.87 | 71.99 |
| | 500 | 30.20 | 2.87 | 73.82 |
| | 1000 | 31.84 | 2.05 | 75.17 |
| | blank | 5.864 | 2.96 | |
| | 100 | 13.12 | 7.01 | 55.30 |
| 50 | 250 | 15.56 | 6.77 | 62.31 |
| | 500 | 19.91 | 2.30 | 70.54 |
| | 1000 | 20.20 | 2.00 | 71.00 |

## 4. Conclusions

Silane-functionalized $Fe_3O_4$ nanoparticles were studied for their anti-corrosion activity against mild steel in 0.5 M HCl. Ferric oxide nanoparticles and APTES-functionalized magnetite nanoparticles were successfully synthesized via coprecipitation and characterized using SEM and FT-IR. Silane-functionalized $Fe_3O_4$ nanoparticles act as an efficient inhibitor of mild steel in 0.5 M HCl solution. Inhibition efficiency increases with increasing inhibitor concentration and decreases with increasing temperature. Potentiodynamic polarization studies revealed that the $Fe_3O_4$@APTES nanoparticles behave as mixed-type inhibitors. The adsorption of functionalized nanoparticles on a mild steel surface follows the Langmuir adsorption isotherm. Thermodynamic data indicate the presence of both physisorption and chemisorption, with physisorption predominating.

## Funding

This research received no external funding.

## Acknowledgments

Declared none.

## Conflicts of Interest

The authors declare no conflict of interest.

## References

1. Rocha-Santos, T.A.P. Sensors and biosensors based on magnetic nanoparticles. *TrAC - Trends Anal. Chem.* **2014**, *62*, 28–36, https://doi.org/10.1016/j.trac.2014.06.016.
2. Porosoff, M.D.; Chen, J.G. Trends in the catalytic reduction of $CO_2$ by hydrogen over supported monometallic and bimetallic catalysts. *J. Catal.* **2013**, *301*, 30–37, https://doi.org/10.1016/j.jcat.2013.01.022.
3. Barry, N.P.E.; Sadler, P.J. Challenges for Metals in Medicine: How Nanotechnology May Help To Shape the Future. *ACS Nano* **2013**, *7*, 5654–5659, https://doi.org/10.1021/nn403220e.
4. Parveen, S.; Misra, R.; Sahoo, S.K. Nanoparticles: A boon to drug delivery, therapeutics, diagnostics and imaging. *Nanomedicine Nanotechnology, Biol. Med.* **2012**, *8*, 147–166, https://doi.org/10.1016/j.nano.2011.05.016.
5. Mireles, L.-K.; Sacher, E.; Yahia, L.H.; Laurent, S.; Stanicki, D. A comparative physicochemical, morphological and magnetic study of silane-functionalized superparamagnetic iron oxide nanoparticles prepared by alkaline coprecipitation. *Int. J. Biochem. Cell Biol.* **2016**, *75*, 203–211, https://doi.org/10.1016/j.biocel.2015.12.002.
6. Tiwari, S.C.; Tripathi, R.K.; Kumar, A. Applicability of the Mini-mental State Examination (MMSE) and the Hindi Mental State Examination (HMSE) to the urban elderly in India: A pilot study. *Int. Psychogeriatrics* **2009**, *21*, 123–128, https://doi.org/10.1017/S1041610208007916.
7. Ulusoy, E.; Bozkurt, A.; Durmaz, S.; Servi, H.; Vardar, F.; Erisen, S. Impact of silver nanoparticles on secondary metabolite composition and toxicity in anise (*Pimpinella anisum* L. ) callus culture. *BMC Plant Biol.* **2024**, *24*, 362, https://doi.org/10.1186/s12870-024-05067-8.
8. Vedmedenko, E. Competing interactions and pattern formation in nanoworld; John Wiley & Sons: **2007**.
9. Al-darwesh, M.Y.; Ibrahim, S.S.; Mohammed, M.A. A review on plant extract mediated green synthesis of zinc oxide nanoparticles and their biomedical applications. *Results Chem.* **2024**, *7*, 101368, https://doi.org/10.1016/j.rechem.2024.101368.
10. Atta, A.M.; El-mahdy, G.A.; Al-lohedan, H.A.; El-saeed, A.M. Preparation and Application of Crosslinked Poly(sodium acrylate)-Coated Magnetite Nanoparticles as Corrosion Inhibitors for Carbon Steel Alloy. *Molecules* **2015**, *20*, 1244-1261, https://doi.org/10.3390/molecules20011244.
11. Altammar, K.A. A review on nanoparticles: characteristics, synthesis, applications, and challenges. *Front. Microbiol.* **2023**, *14*, 1–20, https://doi.org/10.3389/fmicb.2023.1155622.
12. Paut, A.; Gué, L.; Vrankić, M.; Crnčević, D.; Šenjug, P.; Pajić, D.; Odžak, R.; Šprung, M.; Nakić, K.; Marciuš, M.; Prkić, A.; Mitar, I. Plant-Mediated Synthesis of Magnetite Nanoparticles with Matricaria chamomilla Aqueous Extract. *Nanomaterials* **2024**, *14*, 729, https://doi.org/10.3390/nano14080729.
13. Soltys, L.; Olkhovyy, O.; Tatarchuk, T.; Naushad, M. Green Synthesis of Metal and Metal Oxide Nanoparticles : Principles of Green Chemistry and Raw Materials. *Magnetochemistry* **2021**, *7*, 145, https://doi.org/10.3390/magnetochemistry7110145.
14. Lucchini, M.A.; Riani, P.; Canepa, F. Quantitative analysis of the a.c. susceptibility of core-shell nanoparticles. *J. Nanoparticle Res.* **2013**, *15*, 1601, https://doi.org/10.1007/s11051-013-1601-x.
15. Friedman, M. Applications of the Ninhydrin Reaction for Analysis of Amino Acids, Peptides, and Proteins to Agricultural and Biomedical Sciences. *J. Agric. Food Chem.* **2004**, *52*, 385–406, 2004, https://doi.org/10.1021/jf030490p.
16. Villa, S.; Riani, P.; Locardi, F.; Canepa, F. Functionalization of $Fe_3O_4$ NPs by silanization: Use of amine

(APTES) and thiol (MPTMS) silanes and their physical characterization. *Materials* **2016**, *9*, 826, https://doi.org/10.3390/ma9100826.
17. Atta, A.M.; Al-lohedan, H.A. Application of Eco-friendly Magnetite Nanoparticles Coated with Rosin Amidoxime as Corrosion Inhibitor for Mild Steel in 1 M Hydrochloric Acid Solution. *International Journal of Electrochemical Science* **2015**, *10*, 2621-2633, https://doi.org/10.1016/S1452-3981(23)04873-3.
18. Larabi, L.; Harek, Y.; Benali, O.; Ghalem, S. Hydrazide derivatives as corrosion inhibitors for mild steel in 1 M HCl. *Prog. Org. Coatings* **2005**, *54*, 256–262, https://doi.org/10.1016/j.porgcoat.2005.06.015.
19. Li, W.; He, Q.; Pei, C.; Hou, B. Experimental and theoretical investigation of the adsorption behaviour of new triazole derivatives as inhibitors for mild steel corrosion in acid media. *Electrochimica Acta* **2007**, *52*, 6386-6394, https://doi.org/10.1016/j.electacta.2007.04.077.
20. McCafferty, E.; Hackerman, N. Double Layer Capacitance of Iron and Corrosion Inhibition with Polymethylene Diamines. *Journal of the Electrochemical Society* **1972**, *119*, 146–154, https://iopscience.iop.org/article/10.1149/1.2404150.
21. Lebrini, M.; Bentiss, F.; Vezin, H.; Lagrenée, M. Inhibiting effects of some oxadiazole derivatives on the corrosion of mild steel in perchloric acid solution. *Applied Surface Science* **2005**, *252*, 950–958, https://doi.org/10.1016/j.apsusc.2005.01.160.
22. Quraishi, M.A.; Sharma, H.K. Thiazoles as corrosion inhibitors for mild steel in formic and acetic acid solutions. *Journal of Applied Electrochemistry* **2005**, *35*, 33–39, https://doi.org/10.1007/s10800-004-2055-8.
23. Bouklah, M.; Hammouti, B.; Benkaddour, M.; Benhadda, T. Thiophene derivatives as effective inhibitors for the corrosion of steel in 0.5 M $H_2SO_4$. *Journal of Applied Electrochemistry* **2005**, *35*, 1095–1101, https://doi.org/10.1007/s10800-005-9004-z.
24. Parkins, R.N. Corrosion Inhibition. In Electrochemical Materials Science, Bockris, J.O.M., Conway, B.E., Yeager, E., White, R.E., Eds.; Springer US: Boston, MA, **1981**; pp. 307-331, https://link.springer.com/chapter/10.1007/978-1-4757-4825-3_6.
25. Shukla, S.K.; Quraishi, M.A. Cefotaxime sodium : A new and efficient corrosion inhibitor for mild steel in hydrochloric acid solution. *Corros. Sci.* **2009**, *51*, 1007–1011, https://doi.org/10.1016/j.corsci.2009.02.024.
26. Durnie, W.; De Marco, R.; Kinsella, B.; Jefferson, A.; Pejcic, B. Predicting the Adsorption Properties of Carbon Dioxide Corrosion Inhibitors Using a Structure-Activity Relationship. *Journal of the Electrochemical Society* **2005**, *152*, B1, https://doi.org/10.1149/1.1823991.
27. Gomma, G.K.; Wahdan, M.H. Schiff bases as corrosion inhibitors for aluminium acid solution in hydrochloric. *Materials* **1995**, *39*, 209-213, https://doi.org/10.1016/0254-0584(94)01436-K.
28. Şahin, M.; Bilgiç, S.; Yılmaz, H. The inhibition effects of some cyclic nitrogen compounds on the corrosion of the steel in NaCl mediums. *Applied Surface Science* **2002**, *195*, 1–7, https://doi.org/10.1016/S0169-4332(01)00783-8.
29. Olivares-Xometl, O.; Likhanova, N.V.; Domínguez-Aguilar, M.A.; Hallen, J.M.; Zamudio, L.S.; Arce, E. Surface analysis of inhibitor films formed by imidazolines and amides on mild steel in an acidic environment. *Appl. Surf. Sci.* **2006**, *252*, 2139–2152, https://doi.org/10.1016/j.apsusc.2005.03.178.
30. Kumar, C.B.P.; Mohana, K.N.; Muralidhara, H.B. Electrochemical and thermodynamic studies to evaluate the inhibition effect of synthesized piperidine derivatives on the corrosion of mild steel in acidic medium. *Ionics* **2015**, *21*, 263–281, https://doi.org/10.1007/s11581-014-1178-0.
31. Fuchs-Godec, R. The adsorption, CMC determination and corrosion inhibition of some *N*-alkyl quaternary ammonium salts on carbon steel surface in 2 M $H_2SO_4$. *Colloids Surfaces A Physicochem. Eng. Asp.* **2006**, *280*, 130–139, https://doi.org/10.1016/j.colsurfa.2006.01.046.
32. Hosseini, M.G.; Ehteshamzadeh, M.; Shahrabi, T. Protection of mild steel corrosion with Schiff bases in 0.5 M H2SO4 solution. *Electrochim. Acta* **2007**, *52*, 3680–3685, https://doi.org/10.1016/j.electacta.2006.10.041.
33. Singh, A.K.; Quraishi, M.A. Effect of Cefazolin on the corrosion of mild steel in HCl solution. *Corros. Sci.* **2010**, *52*, 152–160, https://doi.org/10.1016/j.corsci.2009.08.050.
34. Amin, M.A.; Abd El-Rehim, S.S.; El-Sherbini, E.E.F.; Mahmoud, S.R.; Abbas, M.N. Electrochimica Acta Pitting corrosion studies on Al and Al – Zn alloys in SCN – solutions. *Electrochimica Acta* **2009**, *54*, 4288–4296, https://doi.org/10.1016/j.electacta.2009.02.076.
35. Saleh, R.M.; Shams El Din, A.M. Efficiency of organic acids and their anions in retarding the dissolution of aluminium. *Corrosion Science* **1972**, *12*, 689–697, https://doi.org/10.1016/S0010-938X(72)91188-2.
36. Atta, A.M.; El-Mahdy, G.A; Al-Lohedan, H.A. Corrosion inhibition efficiency of modified silver

nanoparticles for carbon steel in 1 M HCL. *Int. J. Electrochem. Sci.* **2013**, *8*, 4873–4885.
37. Odusote, J.K.; Asafa, T.B.; Oseni, J.G.; Adeleke, A.A.; Adediran, A.A.; Yahya, R.A.; Abdul, J.M.; Adedayo, S.A. Inhibition efficiency of gold nanoparticles on corrosion of mild steel, stainless steel and aluminium in 1M HCl solution. *Mater. Today Proc.* **2021**, *38*, 578–583, https://doi.org/10.1016/j.matpr.2020.02.984.